

# Conductive Nanocrystalline Niobium Carbide as High-Efficiency Polysulfides Tamer for Lithium-Sulfur Batteries

Wenlong Cai, Gaoran Li, Kailong Zhang, Guannan Xiao, Can Wang, Kefen Ye, Zhongwei Chen,\* Yongchun Zhu,\* and Yitai Qian

Rational design of functional interlayer is highly significant in pursuit of high-performance Li-S batteries. Herein, a nanocrystalline niobium carbide (NbC) is developed via a facile and scalable autoclave technology, which is, for the first time, employed as the advanced interlayer material for Li-S batteries. Combining the merits of strong polysulfides (PS) anchoring with high electric conductivity, the NbC-coated membrane enables efficiently tamed PS shuttling and fast sulfur electrochemistry, achieving outstanding cyclability with negligible capacity fading rate of 0.037% cycle<sup>-1</sup> over 1500 cycles, superb rate capability up to 5 C, high areal capacity of 3.6 mA h cm<sup>-2</sup> under raised sulfur loading, and reliable operation even in soft-package cells. This work offers a facile and effective method of promoting Li-S batteries for practical application.

## 1. Introduction

With the fast expanding market of portable electronics and electric vehicles, the desires for low-cost and high-energy power source have significantly promoted the research on advanced energy storage systems in purpose of succeeding the conventional lithium-ion batteries (LIBs).<sup>[1–5]</sup> Particularly, lithium-sulfur (Li-S) batteries are considered as one of the most promising candidates ascribing to their exceptionally high theoretical specific capacity (1675 mA h g<sup>-1</sup>) and energy density (2600 Wh kg<sup>-1</sup>). However, the electronic/ionic insulation nature of sulfur, the shuttling behavior of the soluble polysulfides (PS) intermediates, and the large volume variation during discharge-charge process result in poor lifespan of Li-S batteries, impeding their practical application.<sup>[6–12]</sup>

Dr. W. L. Cai, Dr. K. L. Zhang, G. N. Xiao, Prof. Y. C. Zhu, Prof. Y. T. Qian  
Hefei National Laboratory for Physical Science at Microscale and Department of Chemistry  
University of Science and Technology of China  
Hefei, Anhui 230026, P. R. China  
E-mail: ychzhu@ustc.edu.cn

Dr. G. R. Li, Prof. Z. W. Chen  
Department of Chemical Engineering  
University of Waterloo  
200 University Avenue West, Waterloo, Ontario N2L 3G1, Canada  
E-mail: zhwchen@uwaterloo.ca

C. Wang, K. F. Ye  
College of Chemical and Biological Engineering  
Zhejiang University  
Hangzhou 310027, P. R. China

 The ORCID identification number(s) for the author(s) of this article can be found under <https://doi.org/10.1002/adfm.201704865>.

DOI: 10.1002/adfm.201704865

In recent decades, multifarious strategies have been proposed to address these problems, among which rational designs of cathode architecture have attracted the most research efforts.<sup>[13–17]</sup> Although advanced cathode constructions have indeed shown admirable effectiveness in promoting the Li-S performance by offering decent conductivity and sulfur confinement, additional measures still need to be taken to cope with the inevitable dissolution and diffusion behaviors of PS anions. In this regard, functional interlayer serves as a promising candidate to address the PS migration issue by establishing a PS barrier against the PS diffusion through the separator and confining the sulfur species within the cathode section. Representatively, Manthiram and Su<sup>[18]</sup> first introduced a nonpolar carbon paper as a functional interlayer in Li-S system and achieved significantly improved battery cyclability. Since then, carbon-based interlayers such as carbonized paper,<sup>[19]</sup> acetylene black mesh,<sup>[20]</sup> and carbonized eggshell membrane,<sup>[21]</sup> have been extensively investigated for impeding PS migration. Simultaneously, non-carbon interlayers recently are drawing increasingly research attentions as an alternative powerful PS barrier.<sup>[22,23]</sup> For example, a simple surface coating of cation exchange resin such as Nafion on the conventional polyolefins separator was reported with high-efficiency PS blocking and anode protection attributed to the favorable cation selectiveness of the coating layer.<sup>[22]</sup> Although these interlayer strategies have achieved good progress on battery performance, some critical issues remain to be solved: (1) the nonpolar carbon interlayers can only act as a buffer for hindering PS migration, which is incapable of providing adequately strong sulfur confinement particularly for long-term battery operation due to its lack of chemical interaction with polar PS anions; (2) with regard to polar non-carbon interlayers, while the favorable chemical interactions enable good PS blocking, their general insufficiency of both electronic and ionic conductivities lead low sulfur utilization, increased internal resistance, and poor electrochemical kinetics. Therefore, rational interlayer designs combining strong PS blocking and decent conductivity are of profound significance in pursuit of high-performance Li-S batteries for practical application.<sup>[24]</sup>

MXenes, namely, the transition metal carbides, carbonitrides, and nitrides, are drawing a research fever due to their unique electronic, mechanical, and optical properties.<sup>[25]</sup> Among them, niobium carbide (NbC) delivers high electrical conductivity up to  $2.9 \times 10^6$  S m<sup>-1</sup> and excellent mechanical

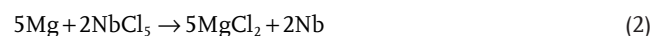
and chemical stabilities,<sup>[26–29]</sup> while its polar molecular structure could offer strong chemical interactions with PS anions, hence NbC serves as a highly potential interlayer material for Li-S batteries. However, traditional synthesis of NbC generally involves high-temperature annealing over 1000 °C and suffers from low yields, poor crystallization, inconvenient manipulations,<sup>[30,31]</sup> which are highly challenging for large-scale application. Herein, a facile autoclave technology was employed to synthesize nanocrystalline NbC through a magnesiothermic reaction at 600 °C. When applied as functional interlayer, the NbC-coated membrane (NCM) anchored PS anions on its surface via strong chemical interactions, thereby confining sulfur within the cathodic section and protecting lithium anode from PS shuttling corrosion. Meanwhile, the highly conductive NCM serves as inner current collector for accelerated sulfur electrochemistry, thus contributing to the enhanced sulfur utilization and improved rate capability. Based on these superiorities, NCM enables simple S/C cathode to achieve outstanding cyclability over 1500 cycles, excellent rate capability up to 5 C, and high areal capacity of 3.6 mA h cm<sup>-2</sup> under raised sulfur loading (4 mg cm<sup>-2</sup>) in coin cell, as well as a reliable operation in soft package. These superb electrochemical performances signify the great potential of NCM separator in practical application of Li-S batteries.

## 2. Results and Discussion

The synthetic procedures of the NbC are illustrated in **Scheme 1**. As presented, the NbC was prepared through a one-pot magnesiothermic reduction of NbCl<sub>5</sub> and CCl<sub>4</sub> in a sealed autoclave under a relatively low temperature of 600 °C.

To understand the synthetic mechanism herein, additional parallel experiments were carried out. First, magnesiothermic reductions were performed for single NbCl<sub>5</sub> or CCl<sub>4</sub>, respectively, under the same conditions. As shown in Figure S1 (Supporting Information), the main reaction product between Mg and NbCl<sub>5</sub> after washing can be indexed to metallic Nb (JCPDS No. 01-089-5008), while the magnesiothermic product of CCl<sub>4</sub> was assigned to carbon (JCPDS No. 01-075-2078). Moreover, Figure S1b (Supporting Information) shows that the products during the co-reduction match well with NbC and MgCl<sub>2</sub>·6H<sub>2</sub>O

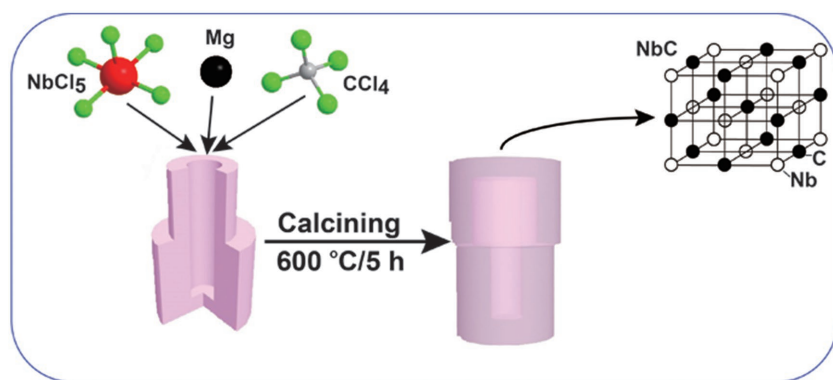
(JCPDS No. 01-074-1039). Hence, the possible mechanism of NbC formation is proposed as follows



It is also found that the reaction time has significant influence on the composition of the product from the co-reduction (Figure S2, Supporting Information). When the magnesiothermic reaction proceeded for 1 h, the product was impure and poorly crystallized. Conversely, when the reaction time was prolonged excessively to 10 h, the side product of Nb<sub>2</sub>C (JCPDS No. 01-077-0988) would appear, which was much less conductive than NbC.<sup>[27]</sup> Therefore, we chose 5 h as the optimum reaction time for synthesis of pure cubic phase (Fm-3m) NbC (JCPDS No. 03-065-7964, *a* = *b* = *c* = 4.43 Å). The conductivity of as-prepared NbC is measured ≈916.8 S m<sup>-1</sup> by four-point probe method, which nearly quintuples that of the super P (SP, 203.5 S m<sup>-1</sup>, measured under the same conditions). It should be noted that the lower conductivity comparing to the value in literature may result from the different testing method and condition.<sup>[29]</sup>

The morphology of the synthesized NbC material was observed by scanning electron microscope (SEM) and transmission electron microscopy (TEM) measurements. It can be clearly seen that the NbC shows basically uniform sphere structure within a size range of 50–100 nm (**Figure 1a,b**). The high-resolution transmission electron microscopy (HRTEM) image shown in **Figure 1c** clearly displays the lattice fringes spacing for (111) and (200) plane of cubic NbC (*d*<sub>111</sub> = 0.257 nm and *d*<sub>200</sub> = 0.22 nm), confirming the presence of highly crystallized NbC. TEM elemental mappings (**Figure 1d**) confirm the homogeneous distribution of Nb and C in the material. The surface chemistry of NbC was studied by X-ray photoelectron spectroscopy (XPS) analysis. As shown in **Figure S3** (Supporting Information), the peaks at 204 and 206.7 eV are assigned to the Nb–C bonding, and the other pair of peaks (207.8 and 210.6 eV) mainly relates to Nb<sub>2</sub>O<sub>5</sub>, which is resulted from the partial passivation of the ambient on the outermost surface of NbC. Such phenomenon can also be commonly observed in other syntheses of NbC.<sup>[32,33]</sup>

The possible chemical interaction between NbC and PS was investigated to explore feasibility of NbC as functional interlayer for Li-S batteries. First, the N<sub>2</sub> adsorption/desorption isotherms and the corresponding pore size distribution of NbC were measured as shown in **Figure S4** (Supporting Information). The pore size distribution indicates that there is almost no micropore in the obtained NbC. The Brunner–Emmet–Teller (BET) specific surface area and total pore volume of NbC



**Scheme 1.** Schematic illustration of the preparation of NbC.

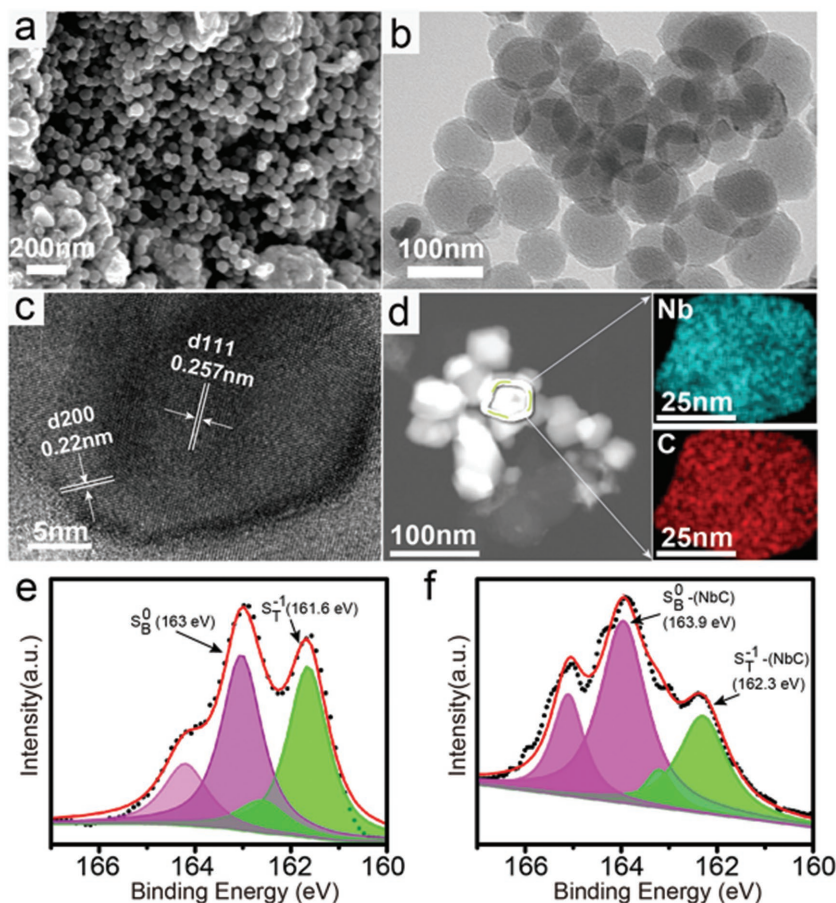


**Figure 1.** a) SEM image, b) TEM image, c) HRTEM image, d) TEM image and the elemental mapping images taken from the selected area, and high-resolution S 2p XPS spectrum of e)  $\text{Li}_2\text{S}_4$  and f)  $\text{NbC-Li}_2\text{S}_4$ .

are calculated as  $22.37 \text{ m}^2 \text{ g}^{-1}$  and  $0.078 \text{ cm}^3 \text{ g}^{-1}$ , respectively. The low porosity of NbC suggests that there is barely spatial confinement for PS. Then, visual discrimination and XPS measurements were combined to probe the chemical interactions. Certain amount of commercial SP ( $62 \text{ m}^2 \text{ g}^{-1}$ ) and NbC with nearly the same total surface area were added in a series of PS ( $\text{Li}_2\text{S}_4$ ,  $\text{Li}_2\text{S}_6$ ,  $\text{Li}_2\text{S}_8$ ) in tetrahydrofuran (THF) solutions, respectively, in order to avoid the contribution of surface area. It is clearly observed that NbC converts all the light yellow  $\text{Li}_2\text{S}_4$ ,  $\text{Li}_2\text{S}_6$ , and  $\text{Li}_2\text{S}_8$  solutions to almost completely transparent after adsorption for 20 min, while color change is barely observed for PS solution with SP absorbent even after 10 h (Figure S5, Supporting Information). As shown in Figure S6b (Supporting Information), no obvious change in peak position is detected, suggesting no phase change of PS anions due to the fact that each PS phase has its characteristic peak in UV-vis spectra.<sup>[34–36]</sup> Based on the UV-vis results, the adsorption capability of NbC is calculated as  $4.856 \text{ mg Li}_2\text{S}_4$  per  $15 \text{ mg}$  of NbC, which is one order higher than that of SP ( $0.369 \text{ mg Li}_2\text{S}_4$  per  $15 \text{ mg}$ ) (Figure S6, Supporting Information), indicating the superior adsorption capability of NbC than SP which performs almost pure physical adsorption. This adsorption is further analyzed by XPS spectra with  $\text{Li}_2\text{S}_4$  as the representative lithium polysulfides. The spectrum of pure  $\text{Li}_2\text{S}_4$  displays two 2p3/2 contributions

assigned to the terminal ( $\text{S}_\text{T}^{-1}$ , 161.6 eV) and bridging sulfur ( $\text{S}_\text{B}^0$ , 163 eV), respectively (Figure 1e). By contrast, the S2p spectrum of the adsorbed  $\text{Li}_2\text{S}_4$  on NbC surface exhibits different chemical status (Figure 1f) with two 2p3/2 contributions at 162.3 and 163.9 eV, representing a +0.7 and +0.9 eV shift for  $\text{S}_\text{T}^{-1}$  and  $\text{S}_\text{B}^0$ , respectively.<sup>[37–39]</sup> Moreover, the PS-adsorbed NbC also shows a +0.4 eV shift for Nb–C bond in the Nb3d spectra (Figure S7, Supporting Information), which further supports the chemical adsorption instead of phase change reaction that interacts between NbC and PS species, because crystalline NbC phase is highly stable. These results essentially support the strong chemical adsorption of NbC to PS, indicating its great potential in hindering the PS shuttling in Li-S batteries.

Based on the above results, NbC was coated on the conventional celgard separator as a functional interlayer for Li-S batteries. Figure 2a depicts a comparison schematic between conventional Li-S configuration with celgard separator and advanced Li-S cell with NCM separator. The photographs of the front and back sides of both the celgard and NCM separators are shown in Figure 2b,c. SEM images of pristine celgard and NCM are presented in Figure 2d–g. It can be seen that pristine celgard surface possesses abundant pores with diameters up to several hundred nanometers (Figure 2d), where the dissolved PS can easily pass through. After coated with NbC (Figure 2f), the pores are well covered which is confirmed via BET measurement (Figure S8, Supporting Information). The cross-section images (Figure 2e,g) depict that the NCM is tightly coated with a dense thin NbC layer of around  $10 \mu\text{m}$ . The total mass loading of coating is  $\approx 0.9 \text{ mg cm}^{-2}$  with a NbC loading of  $0.54 \text{ mg cm}^{-2}$ . The electrochemical impedance spectroscopy (EIS) analysis (Figure S9, Supporting Information) discloses that the  $\text{Li}^+$  conductivity of NCM ( $0.531 \text{ mS cm}^{-1}$ ) is higher than that of celgard ( $0.325 \text{ mS cm}^{-1}$ ), which supports the fast and high-efficiency sulfur electrochemistry. Contrast to the pristine celgard, the NCM separator is able to impede the PS penetration through the separator and trap PS within the cathode section benefiting from the strong interactions between NbC and PS, thereby significantly suppressing the PS shuttling behavior in Li-S batteries. Meanwhile, the long-term cyclability and good rate capability of the corresponding batteries can also be obtained due to the excellent electric conductivity of NbC.

Electrochemical evaluations were performed to investigate the functions of NCM separator in Li-S batteries. S/C composite prepared by simply mixing the elemental sulfur and SP was applied as the cathode material. Thermogravimetric analysis (TGA, Figure S10, Supporting Information) confirms the sulfur content in the S/C composite is 66.7 wt%, corresponding to a sulfur content in the whole cathode of 60 wt%. The areal sulfur loading in cathode is about  $1.5 \text{ mg cm}^{-2}$ . As

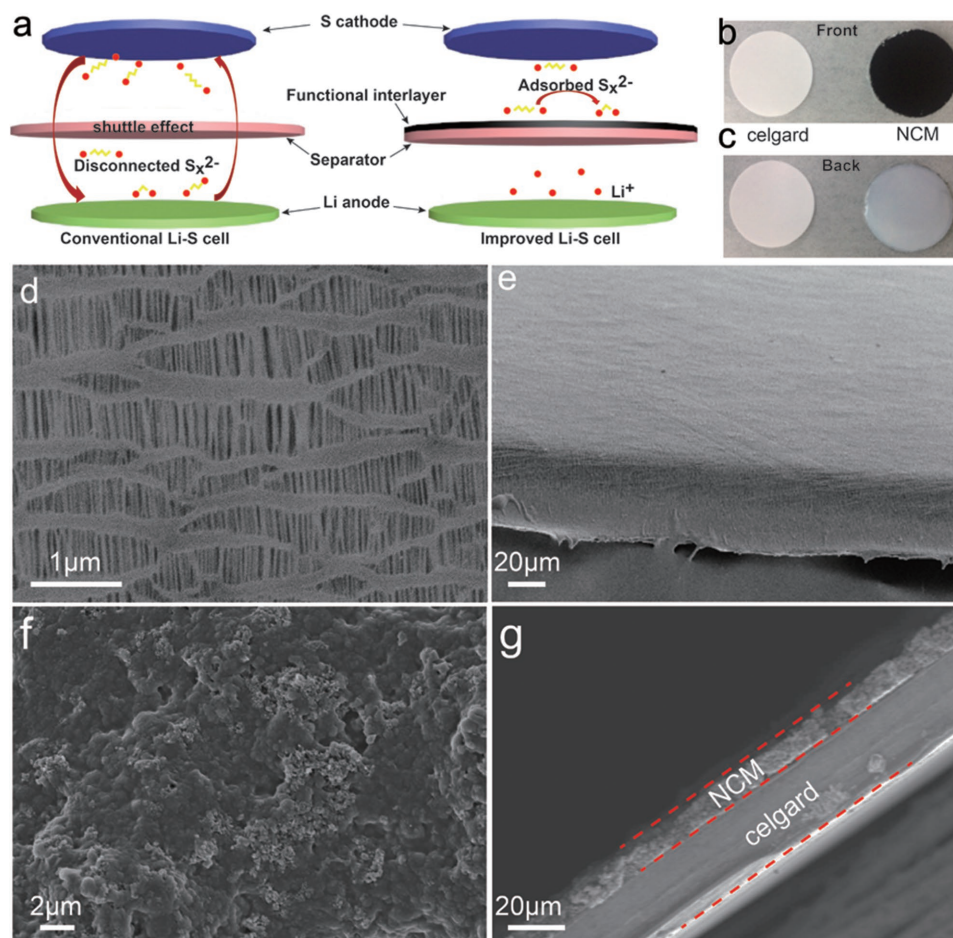


**Figure 2.** a) Schematic diagram of conventional Li-S cell and improved Li-S cell; photographs of the b) front and c) back of the celgard (left) and NCM (right); SEM images of d) top surface and e) cross section of celgard; and f) top surface and g) cross section of NCM.

depicted in the cyclic voltammograms (CV) curves at a scan rate of  $0.1 \text{ mV s}^{-1}$  (Figure 3a), the two cathodic peaks at around 2.3 and 2.04 V correspond to the reduction of element sulfur to high-order PS ( $\text{Li}_2\text{S}_x$ ,  $4 \leq x \leq 8$ ) and further conversion into lithium sulfides ( $\text{Li}_2\text{S}/\text{Li}_2\text{S}_2$ ), respectively, while the strong broad peak and the shoulder peak around 2.3 and 2.36 V in the subsequent anodic scan are assigned to the reverse oxidation reductions. Comparing to that with celgard separator, the CV curves of NCM-based cell show higher electrochemical stability and distinctly lower polarization, suggesting its fast reaction kinetic (Figure S11, Supporting Information). Consistent with the CV curves, the galvanostatic charge–discharge profiles (Figure 3b) exhibit two reduction plateaus and two oxidation plateaus, representing the typical redox reactions of Li-S battery.

Moreover, the cycling performances of the conventional and improved Li-S cells at a current rate of 0.2 C ( $1 \text{ C} = 1675 \text{ mA mg}^{-1}$ ) are presented in Figure S12a (Supporting Information) and Figure 3c. The cell with NCM exhibits higher initially discharge capacity of  $1304.3 \text{ mA h g}^{-1}$  than that based on conventional celgard separator ( $1040.3 \text{ mA h g}^{-1}$ ). The retained capacity after 100 cycles is  $988.4 \text{ mA h g}^{-1}$  for NCM, which indicates its smaller capacity decay rate of 0.24% than that for celgard (0.497%). To clarify the capacity contribution

from NCM, the cell with only NCM separator and lithium anode but no sulfur cathode was measured under the same condition. The result reveals a negligible capacity of  $10 \text{ mA h g}^{-1}$  for pure NCM, suggesting that NCM barely contribute capacity to the improved Li-S system (Figure S12b, Supporting Information). The long-term cycling performance of Li-S cells with NCM separator was also tested at 0.5, 1, and 2 C, respectively. As displayed in Figure 3d, a capacity of  $1082 \text{ mA h g}^{-1}$  is obtained at 0.5 C after the activation in the first two cycles at 0.1 C. A highly reversible capacity of  $872 \text{ mA h g}^{-1}$  is retained after 150 cycles with a high capacity retention of 80.6%. Notably, the NCM-based cell exhibits outstanding cyclability by maintaining a high capacity of around  $750 \text{ mA h g}^{-1}$  after 500 cycles at 1 C (Figure S12c, Supporting Information), and  $500 \text{ mA h g}^{-1}$  with an exceptionally low fading rate of 0.037% over 1500 cycles at 2 C (Figure 3e). The Li-S cell with NCM separator shows highly competitive performance compared with those reported in the recent publications based on interlayer technology and pure sulfur cathode (Table S1, Supporting Information). The superior cyclability of Li-S batteries based on NCM interlayer is attributed to its strong chemical adsorption to PS anions as verified above, which effectively blocks the migration of PS through the separator and confine them within the cathode section for

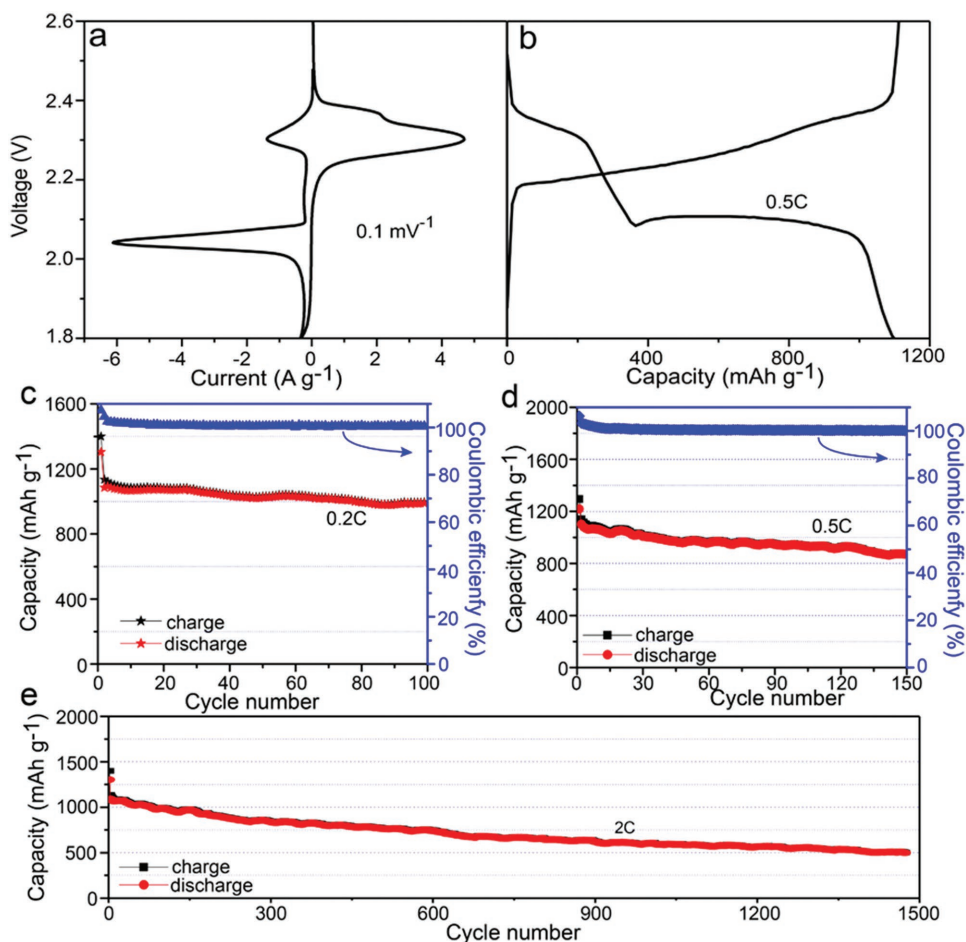


**Figure 3.** a) CV curves at a scan rate of  $0.1 \text{ mV s}^{-1}$  and b) charge–discharge curves at  $0.5 \text{ C}$  of the cell with NCM. Cycling performance of the cells with NCM at a current of c)  $0.2$ , d)  $0.5$ , and e)  $2 \text{ C}$ .

enhanced sulfur utilization. Moreover, the high conductivity of NbC also favors the fast and thorough sulfur electrochemistry so as to achieve the highly durable battery operation.

To investigate the superiorities of NCM separator for the sulfur redox kinetics, batteries were evaluated at different current range from  $0.2$  to  $5 \text{ C}$ . Given the inherently poor electric conductivity of sulfur and celgard separator, the battery with the celgard shows fast capacity decay along with the increase of testing current. When the conductive NCM separator was applied (Figure 4a), the additional electron path leads to high utilization of the active materials (Figure S13a, Supporting Information) and facilitated electrochemical reversibility, which enables extremely high discharge capacities of  $840$  and  $730 \text{ mA h g}^{-1}$  at  $2$  and  $5 \text{ C}$ , respectively. When the testing current is recovered to  $0.2 \text{ C}$ , a high reversible capacity of  $980 \text{ mA h g}^{-1}$  can still be achieved. The corresponding charge–discharge voltage profiles at different rates are depicted in Figure 4b,c. Even at  $5 \text{ C}$ , the two discharge plateaus can still be clearly observed at  $2.3$  and  $2.0 \text{ V}$  corresponding to the two-stage electrochemical sulfur reduction in the voltage profile of the cell based on NCM separator, while almost no plateaus can be observed in that with celgard separator. Besides, the cell with NCM shows significantly smaller voltage hysteresis at high

rates compared with the cell with celgard (Figure 4d), indicating its much easier electrochemical redox reaction at high rates.<sup>[40]</sup> The discharge capacity at the higher discharge voltage plateau ( $Q_H$ ) is often used to evaluate the extent of PS generation and the PS trapping capabilities of cells.<sup>[41,42]</sup> The higher  $Q_H$  with NCM indicates that the soluble PS are effectively retained in cathodic side, and the sulfur loss caused by the diffusion of the dissolved PS are greatly impeded by the NCM interlayer (Figure S13b, Supporting Information). In addition, the lower capacity ratio of high plateau to low plateau ( $Q_H/Q_L$ ) (Figure 4e) for cell with NCM manifests the improved conversion of PS to the final  $\text{Li}_2\text{S}_2/\text{Li}_2\text{S}$ , suggesting that the conductive NCM can facilitate the reduction of PS. The EIS spectra of the electrodes with different separators before and after cycles also reveal that NCM could promote sulfur species lithiation as verified by its much lower charge-transfer resistance, which confirms its much improved reaction kinetics for sulfur electrochemistry (Figure S14, Supporting Information).<sup>[43]</sup>

Moreover, the self-discharge property is another critical index for practical application of Li-S batteries. During the resting time, the solvation and diffusion of sulfur or PS species would lead to severe self-discharge behavior for the batteries, resulting in decreased of open-circuit voltage (OCV) and

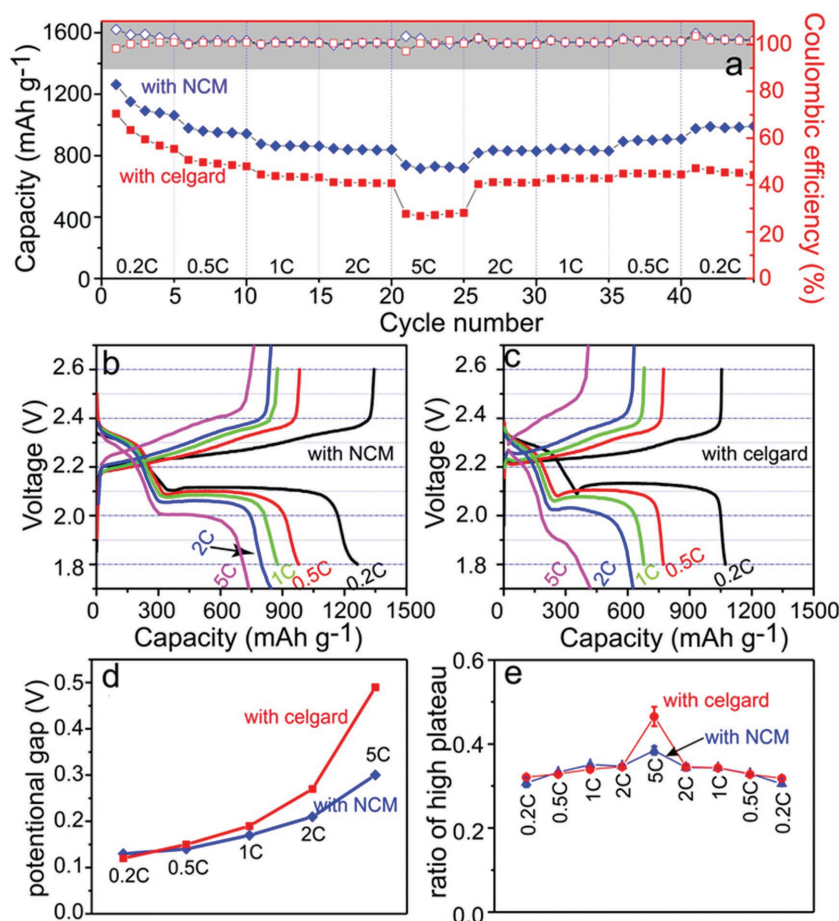


**Figure 4.** a) Rate performance of the electrodes with celgard and NCM, galvanostatic charge–discharge profiles at various rate of battery b) with NCM and c) with celgard. d) The potential gap at various rates of the cells with celgard and NCM. e) The ratio of high plateau of the cells with celgard and NCM.

irreversible capacity decay.<sup>[44–46]</sup> Thus, the capacity loss during the open-circuit interruption is a powerful indicator of the self-discharge behavior as well as the inhibition of PS shuttling in Li-S batteries.<sup>[47]</sup> The self-discharge behaviors of Li-S batteries based on different separators were first studied by discharging the cells to 2.15 V and rest for 10 h in each cycle (Figure S15, Supporting Information). Compared with that based on celgard separator, cell with NCM shows almost no capacity loss in first four cycles, indicating its stronger ability to hinder the shuttling effect. Apart from that, the cells were further rested for 40 h after the fourth charge as illustrated in Figure 5a–d. In the case of celgard, the subsequent discharge after the cell rest shows a low initial voltage of 2.25 V (Figure 5a) and a single low-potential plateau (Figure 5c, green line), while the discharge capacity reduces to only 59.77% of its fourth cycle. By contrast, the NCM-based cell exhibits a much higher initial voltage of 2.33 V (Figure 5b) and a typical two-plateau discharge profile (Figure 5d, green line) with a high capacity retention of 86.88%. This result reveals that the cell with the pristine separator suffers severe self-discharge caused by the dissolution and shuttling of PS in the electrolyte,<sup>[48]</sup> while such problem can be well remitted by the NCM separator. Furthermore, the different

separators were disassembled after cycling and subsequently dipped in THF solution to evaluate their PS adsorption capability. It can be clearly observed that the solution with celgard turns pale yellow immediately after the separator immersion, while the solution with NCM maintains transparent (Figure 5e). UV–vis spectra (Figure 5f) further reveal the much higher PS concentration in solution with celgard contains, and confirms the much higher capability of retaining PS in NCM.<sup>[23]</sup>

The PS blocking effect of NCM separator was further studied in more intuitionistic ways as shown in Figure 6a and Figure S16 (Supporting Information). In Figure 6a, the device is composed by inverting a small bottle containing lithium polysulfides solution inside a big bottle containing fresh electrolyte. The two bottles are separated by different membranes (i.e., celgard and NCM). The diffusion behavior of PS can be clearly observed through the color change in the big bottle. In the case of celgard separator, the PS began to diffuse through the separator and into the fresh electrolyte after dipping the small bottle in the big one for 1 h as the color of the fresh electrolyte turns obviously yellow. The color turns even deeper after 2 h because of the rapid PS diffusion along the concentration gradient. In striking contrast, the fresh electrolyte in the set with NCM maintains transparent after 2 h and turns pale yellow after 3 h diffusion, indicating the much superior capability of resisting PS diffusion for the NCM separator. Moreover, as shown in a visible H-type glass cell (Figure S16, Supporting Information),<sup>[22]</sup> it is obvious that PS leaches from the sulfur electrode and darkens the electrolyte color from 0 min to 8 h for both cells with celgard or NCM. After 12 h discharge with celgard, the PS pass through the celgard to lithium anode and the color of two sides are the very close after 20 h. As for the cell with NCM, the color of the anodic section remains transparent even after 20 h, suggesting that NCM delivers much higher capability of confining PS in cathodic side and taming the PS shuttling behavior than conventional celgard separator. Apart from that, the surface morphologies of lithium anodes after cycling are further characterized as an indicator of PS shuttling and PS blocking effects in coin cells with different separators. As shown in Figure 6b,c, the morphology of the pristine Li anode is smooth and flat. However, the cycling based on celgard separator (Figure 6d,e) give rise to a rough surface with large number of bulges and cracks. Comparatively, the lithium anode cycled with NCM separator delivers a much smoother surface (Figure 6f,g), indicating the much stronger anode protection of NCM by impeding the diffusion of PS anions through the separator. Moreover, the SEM observation clearly shows the particle deposition on both sides of the celgard separator (Figure S17e,g, Supporting Information), while the deposition

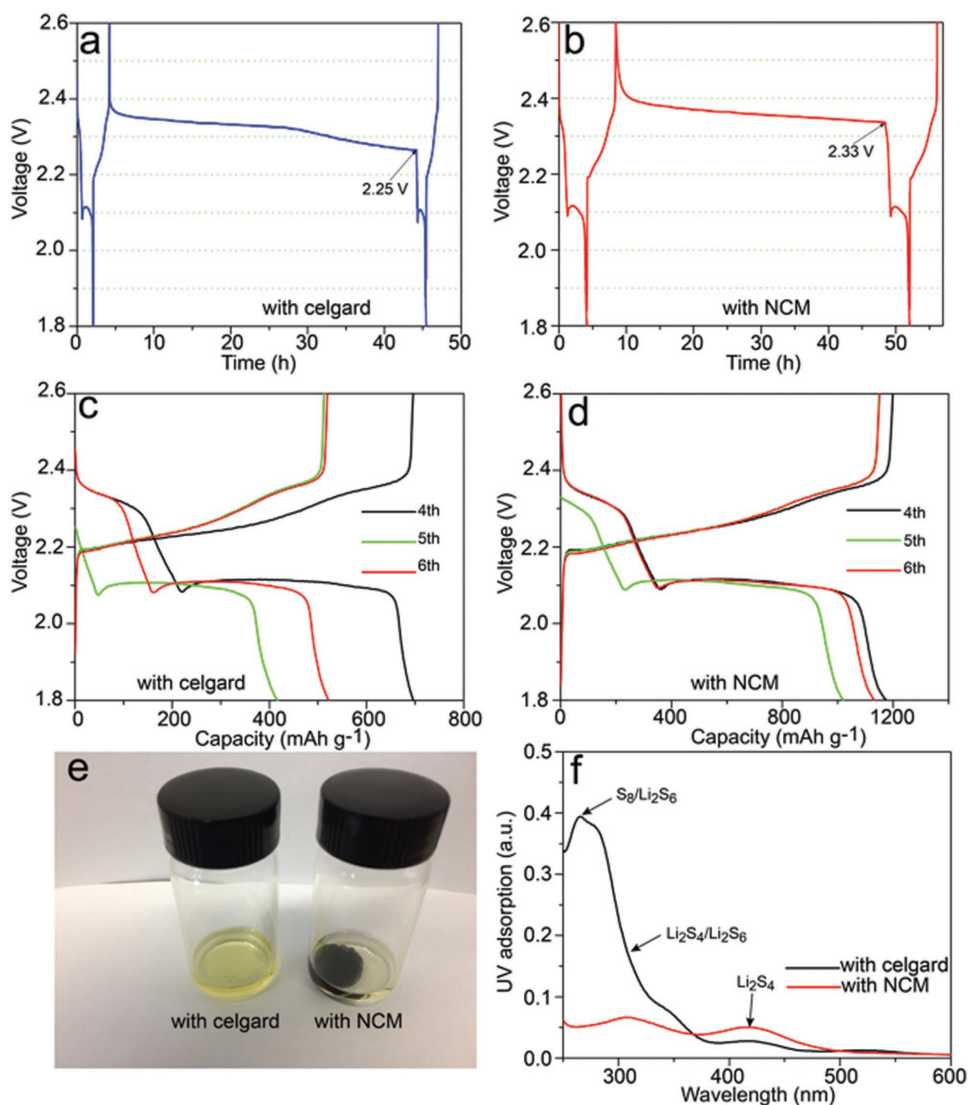


**Figure 5.** The fourth and fifth voltage–time profiles of the cells a) with celgard and b) with NCM, the fourth, fifth, and sixth charge–discharge voltage profiles of the cells c) with celgard and d) with NCM, all the cells are resting for 40 h before the fifth discharge. e) The photo of the cycled separators soaked in THF solution and f) corresponding UV–vis spectra.

can only be found on the coating side of the NCM (Figure S17a, Supporting Information). The NCM separator shows a smooth surface on the side toward the anode (Figure S17c, Supporting Information). In addition, the energy-dispersive X-ray (EDX) spectroscopy measurements (Figure S17, Supporting Information) also reveal the much lower S content on the NCM surface toward anode than that on the surface toward cathode, while the sulfur content on the two sides of the celgard separator are very close. This result demonstrates that NCM can successfully confine PS in the cathodic side and prevent lithium anode from passivation. Thus, the excellent performance of Li-S batteries with NCM separator can be ascribed to: (1) the NCM interlayer with strong PS adsorption is capable of inhibiting PS shuttling behaviors; (2) the NCM interlayer confines PS within the cathode side, thus decreasing the battery self-discharging behavior and protecting lithium anode from side reactions; (3) the conductive NCM provides rapid electron transfer to

accelerate the electrochemical redox of the soluble intermediates and enhance the sulfur utilization.

High sulfur loading is necessary for Li-S batteries to meet the commercial requirements. Armed with the abovementioned superiorities, NCM delivers good potential to support higher sulfur loading. Herein, we prepared thick cathodes with a sulfur loading about  $4 \text{ mg cm}^{-2}$  for the high-loading measurements. As shown in Figure 7a, the thick sulfur electrode with NCM separator delivers an initial area capacity of  $2.48 \text{ mA h cm}^{-2}$  at  $0.2 \text{ C}$ , which increases to  $3.6 \text{ mA h cm}^{-2}$  after several cycles' activation. Even after 47 cycles, a capacity of  $3.48 \text{ mA h cm}^{-2}$  can still be maintained. When current density is raised to  $0.5 \text{ C}$ , typical two-plateau voltage profile can still be obtained as displayed in Figure 7b. Figure 7c shows the long-term galvanostatic cycling at  $0.5 \text{ C}$  after 5 cycles' activation at  $0.2 \text{ C}$ . A high capacity retention of 88.5% is achieved over 100 cycles attributed to the high-efficiency inhibition on PS shuttling benefited from NCM

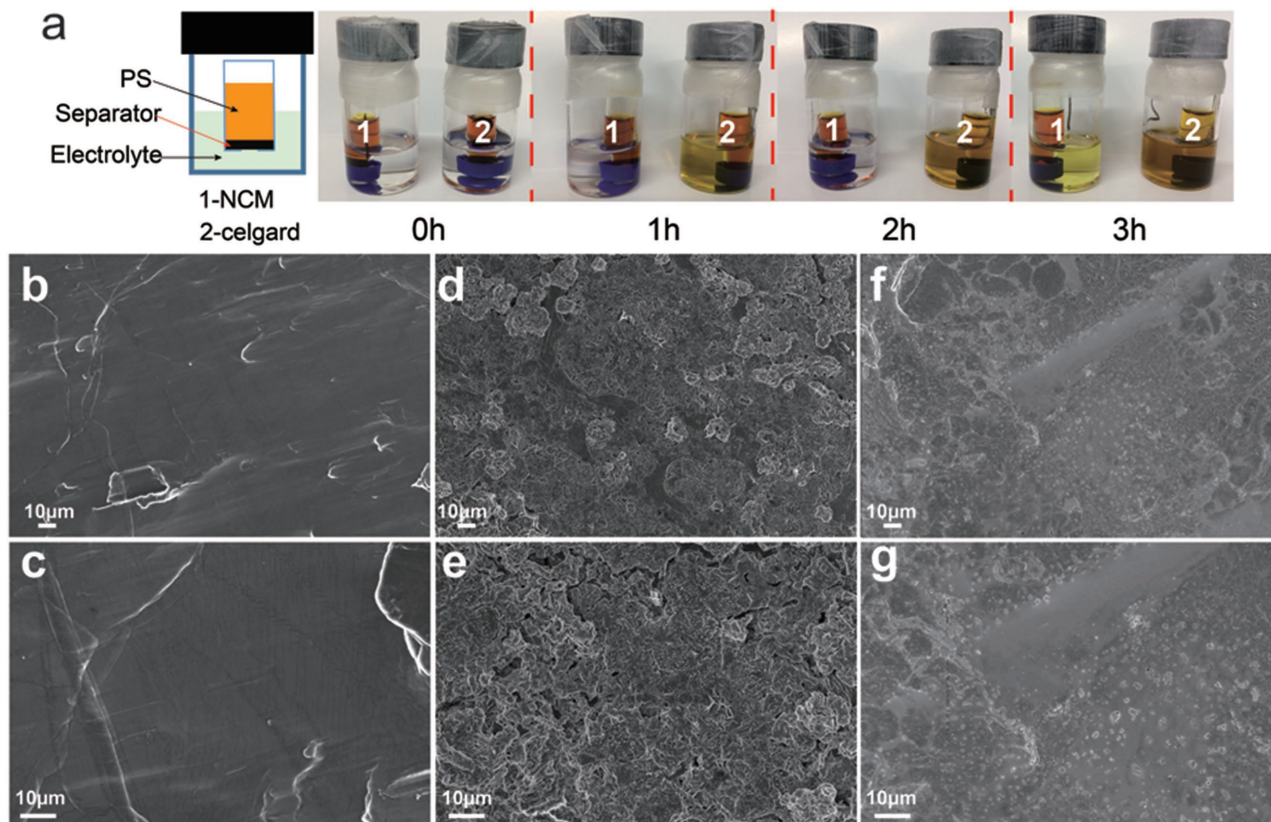


**Figure 6.** a) Visual verification of the diffusion test. Each device comprised PS solution, electrolyte as described in the Experimental Section and different separators. SEM images of the b,c) pristine lithium anode, d,e) cycled lithium anode with celgard separator, and f,g) cycled lithium anode with NCM separator.

separator. By contrast, the coupling of thick cathode with conventional celgard separator (Figure S18, Supporting Information) can only achieve a single charge–discharge plateau and a low areal capacity of  $1.3 \text{ mA h cm}^{-2}$  at  $0.5 \text{ C}$  after 50 cycles due to the severe electrochemical polarization and PS shuttling. It should be noted that extra mass of NbC would decrease the energy density of battery. Concerning this issue, the capacity based on the whole mass loading on the electrode (for celgard-based cell) or that additionally plus the mass of the NCM coating (for NCM-based cell) is shown in Figure S19 (Supporting Information), which indicates that the mass loading of  $0.9 \text{ mg cm}^{-2}$  on NCM is in an acceptable range in improving the energy density of battery. Similar mass loading on functionalized interlayer can also be observed in previous literatures.<sup>[49,50]</sup> These results strongly support that the precious properties including the high conductivity and excellent PS blocking capability of NCM play pivotal roles in promoting the Li-S performance for practical use. The intriguing electrochemical performance has encouraged us to further validate the feasibility of the NCM-based Li-S batteries in a commercial viable prototype. A soft-package Li-S cell with NCM separator was prepared, which was able to light up an LED as shown in Figure 8a. Two prominent discharge plateaus at 2.29 and 2.11 V can be clearly observed in the voltage profile (Figure 8b), indicating its good sulfur electrochemical kinetics. Figure 8c displays an initial capacity of  $1125 \text{ mA h g}^{-1}$  of the soft-package cell, and a stable cyclability over 95 cycles at

$0.2 \text{ C}$ . All these results strongly reveal the appealing superiorities of NCM separator in Li-S batteries to support their potential practical applications.

### 3. Conclusion

In summary, the conductive nanocrystalline NbC was synthesized through a facile and scalable autoclave technology, and for the first time applied as the interlayer material for improved Li-S battery performance. The NCM with high electrical conductivity and strong capability of anchoring PS species was proved to be highly effective in improving the cycling performance and rate capabilities. The conductive NCM interlayer not only serves as shield to confine PS in the cathodic side, which prevents lithium anode from passivation and alleviates the battery self-discharging behavior, but also acts as “second current collector” to reuse the trapped active material and significantly enhance the sulfur utilization. Attributed to these featuring superiorities, the simple S/C cathode with NCM separator achieves an outstanding cyclability with a negligible capacity fading rate of  $0.037\% \text{ cycle}^{-1}$ , high areal capacity of  $3.6 \text{ mA h cm}^{-2}$  under raised sulfur loading, and reliable operation in soft-package cells. This work promotes the pace of Li-S commercialization by offering a facile and cost-efficient method for improved electrochemical performance.

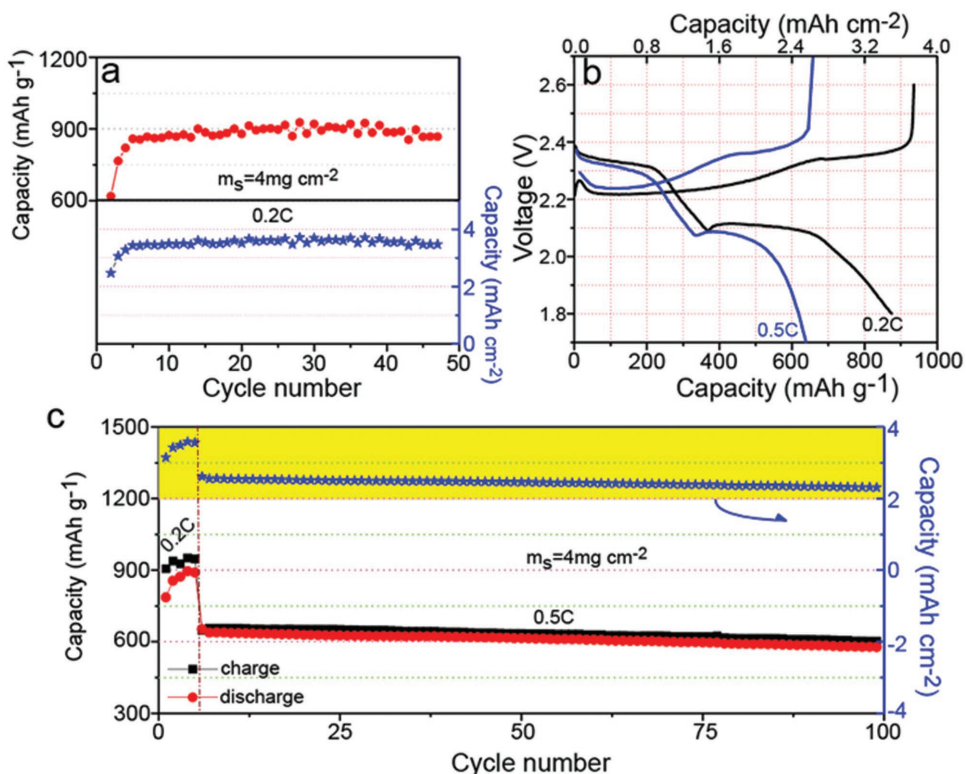


**Figure 7.** a) Cycle performance of the Li-S cell at 0.2 C. b) Charge–discharge voltage profiles of the Li-S cell at 0.2 and 0.5 C. c) Cycle performance of the Li-S cell at 0.5 C. All the cells are with NCM separator and with a sulfur loading of  $\approx 4 \text{ mg cm}^{-2}$ .

#### 4. Experimental Section

**Synthesis of NbC:** NbC was synthesized through the magnesiothermic reduction in autoclave. Typically, equal amount of  $\text{CCl}_4$  (0.01 mol) and  $\text{NbCl}_5$  (0.01 mol), and excess metallic Mg (0.1 mol) were mixed and sealed in a glass lined stainless autoclave. The autoclave was maintained at  $600 \text{ }^\circ\text{C}$  for 5 h and then naturally cooled to room temperature.

The product was collected and washed by absolute ethanol, dilute hydrochloric acid, and deionized water, successively and repeatedly in order to remove the side product. After drying at  $80 \text{ }^\circ\text{C}$  overnight, the final black powder product was collected.

**Fabrication of NCM:** The obtained NbC, SP and poly(vinylidene fluoride) binder (6:2:2 in mass ratio) were dispersed in N-methyl-2-pyrrolidone to form a homogeneous slurry, which was then coated onto

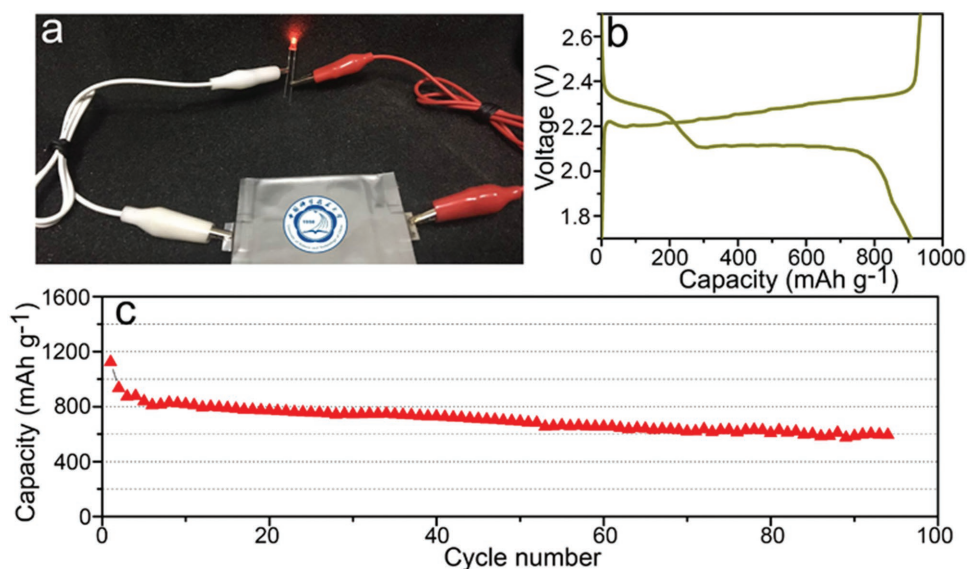


**Figure 8.** a) The photograph of soft package Li-S battery lighting up an LED, b) the charge–discharge curve of the soft package Li-S battery, and c) the cycling performance of soft package Li-S battery at 0.2 C.

the celgard 2400 membrane. The obtained membrane was vacuum dried at 50 °C for 20 h. Finally, the obtained NCM was cut into discs with diameter of 19 mm.

**Preparation of  $\text{Li}_2\text{S}_x$  Solution:** The  $\text{Li}_2\text{S}_4$ ,  $\text{Li}_2\text{S}_6$ , and  $\text{Li}_2\text{S}_8$  solution were prepared by dissolving lithium sulfide (23 mg) and sublimed sulfur (48, 80, and 112 mg) in a molar ratio of 1:3, 1:5, and 1:7 by stoichiometrically in 5 mL anhydrous THF at the same time, respectively. Homogeneous light-yellow  $\text{Li}_2\text{S}_4$ ,  $\text{Li}_2\text{S}_6$ , and  $\text{Li}_2\text{S}_8$  solutions were obtained after vigorous stirring overnight. All the operation was carried in an Ar-filled glove box.

**Determination of Adsorption Amount of  $\text{Li}_2\text{S}_4$ :** The adsorption capability of commercial SP and as-prepared NbC on  $\text{Li}_2\text{S}_4$  was investigated by UV-vis spectroscopy. First, a calibration curve for determination of the concentration was prepared using a set of known concentration  $\text{Li}_2\text{S}_4$  solutions. Then, 15 mg of NbC or SP was added in 2 mL  $\text{Li}_2\text{S}_4$  solution ( $10 \times 10^{-3}$  M) and the mixture was stirred for 10 h, separately. The residual  $\text{Li}_2\text{S}_4$  in the supernatants was collected after centrifugation and solutions were diluted with THF by a factor of 10 to enable quantitative concentration measurements. Based on the calibration curve, the residual concentration of  $\text{Li}_2\text{S}_4$  in the solution was then calculated.

**Coating of S Cathode:** Sulfur and SP (2:1 by mass) were mixed uniformly and sealed in a glass tube, followed by heating at 155 °C in an oven for 12 h. Then the obtained S/C composite (90%) and poly(vinylidene fluoride) binder (10%) in N-methyl-2-pyrrolidinone were mixed to form a homogeneous slurry. The slurry was coated onto aluminum foil by a roll press. And the electrodes were dried in a vacuum oven at 70 °C for 12 h and punched into discs of diameter 12 mm.

**Material Characterization:** X-ray diffraction (XRD) patterns were recorded on a Philips X0 Pert Super diffractometer with Cu K $\alpha$  radiation with  $\lambda = 1.54059$  Å. The morphologies of the samples were characterized by SEM (Zeiss Ultra55) at 5 kV, TEM (Hitachi H7650), and HRTEM (JEM-ARM 200F). Elemental distributions were determined by the EDX (JEM-ARM 200F). The XPS spectra were used to identify surface chemistry by Thermo ESCALAB 250Xi analyzer (Al K $\alpha$  radiation,  $h\nu = 1486.6$  eV). TGA of the S/C composite was performed by TG/DTA 6300 system at a heating rate of 5 °C min $^{-1}$  in N $_2$  flow. The N $_2$  adsorption and desorption isotherms was characterized by an Autosorb-1-C automatic surface and pore-size analyzer (Quatachrome Corp.). UV-vis absorption spectra were conducted to investigate contents of PS species.

**Electrochemical Measurements:** Coin cells (CR2016) were all assembled in Ar-filled glove box by using lithium foil as anode. The electrolyte contains 1 M lithium bis(trifluoromethanesulfonyl)imide (LiTFSI) and 1 wt% LiNO $_3$  in DME-DOL binary solvents (DOL:1,3-dioxolane, DME:1,2-dimethoxyethane, 1:1 ratio in volume). The amount addition was 25 mL g $^{-1}$ S for each cathodes. CV profiles were tested with a scan rate of 0.1 mV s $^{-1}$ . EIS (CHI600D) measurements were carried out from 10 MHz to 0.1 Hz. Galvanostatic charge-discharge was performed within a voltage window of 1.8–2.6 V for regular electrode, and 1.7–2.7 V for thin loading at high rates, high loading at 0.5 C and soft-package cells (with a sulfur loading of  $\approx 2$  mg cm $^{-2}$ ). The current rates and capacities were calculated based on the mass of sulfur. All the electrochemical characterizations were performed at room temperature.

## Supporting Information

Supporting Information is available from the Wiley Online Library or from the author.

## Acknowledgements

The authors would like to appreciate the financial support from the National Natural Science Fund of China (GG2060190212, 21671181, 21471142, and 21521001), Anhui Provincial Natural Science Foundation (1608085MB22), the National Key Research and Development Program of China (2016YFB0901500), and the Fundamental Research Funds for the Central Universities (WK2060190053).

## Conflict of Interest

The authors declare no conflict of interest.

## Keywords

conductive coatings, lithium-sulfur batteries, nanocrystalline niobium carbide, polysulfides tamers

Received: August 23, 2017

Revised: September 30, 2017

Published online: November 16, 2017

- [1] L. Qie, A. Manthiram, *Adv. Mater.* **2015**, *27*, 1694.
- [2] X. L. Huang, D. Xu, S. Yuan, D. L. Ma, S. Wang, H. Y. Zheng, X. B. Zhang, *Adv. Mater.* **2014**, *26*, 7264.
- [3] X. Liang, C. Hart, Q. Pang, A. Garsuch, T. Weiss, L. F. Nazar, *Nat. Commun.* **2015**, *6*, 5682.
- [4] Q. C. Liu, J. J. Xu, S. Yuan, Z. W. Chang, D. Xu, Y. B. Yin, L. Li, H. X. Zhong, Y. S. Jiang, J. M. Yan, X. B. Zhang, *Adv. Mater.* **2015**, *27*, 5241.
- [5] X. Y. Yang, J. J. Xu, D. Bao, Z. W. Chang, D. P. Liu, Y. Zhang, X. B. Zhang, *Adv. Mater.* **2017**, *29*, 1700378.
- [6] Z. A. Ghazi, X. He, A. M. Khattak, N. A. Khan, B. Liang, A. Iqbal, J. X. Wang, H. Sin, L. S. Li, Z. Y. Tang, *Adv. Mater.* **2017**, *29*, 1606817.
- [7] Y. Y. Mao, G. R. Li, Y. Guo, Z. P. Li, C. D. Liang, X. S. Peng, Z. Lin, *Nat. Commun.* **2017**, *8*, 14628.
- [8] J. J. Xu, Q. C. Liu, Y. Yu, J. Wang, J. M. Yan, X. B. Zhang, *Adv. Mater.* **2017**, *29*, 1606552.
- [9] W. L. Cai, J. B. Zhou, G. R. Li, K. L. Zhang, X. Y. Liu, C. Wang, H. Zhou, Y. C. Zhu, Y. T. Qian, *ACS Appl. Mater. Interfaces* **2016**, *8*, 27679.
- [10] G. R. Li, M. Ling, Y. F. Ye, Z. P. Li, J. H. Guo, Y. F. Yao, J. F. Zhu, Z. Lin, S. Q. Zhang, *Adv. Energy Mater.* **2015**, *5*, 1500878.
- [11] G. R. Li, C. Wang, W. L. Cai, Z. Lin, Z. P. Li, S. Q. Zhang, *NPG Asia Mater.* **2016**, *8*, 317.
- [12] W. B. Kong, L. J. Yan, Y. F. Luo, D. T. Wang, K. L. Jiang, Q. Q. Li, S. S. Fan, J. P. Wang, *Adv. Funct. Mater.* **2017**, *27*, 1606663.
- [13] H. J. Peng, J. Q. Huang, M. Q. Zhao, Q. Zhang, X. B. Cheng, X. Y. Liu, W. Z. Qian, F. Wei, *Adv. Funct. Mater.* **2014**, *24*, 2772.
- [14] J. Wang, J. Yang, J. Xie, N. Xu, *Adv. Mater.* **2002**, *14*, 963.
- [15] J. W. Zhou, R. Li, X. X. Fan, Y. F. Chen, R. D. Han, W. Li, J. Zheng, B. Wang, X. G. Li, *Energy Environ. Sci.* **2014**, *7*, 2715.
- [16] L. M. Jin, F. He, W. L. Cai, J. X. Huang, B. H. Liu, Z. P. Li, *J. Power Sources* **2016**, *328*, 536.
- [17] F. F. Zhang, X. B. Zhang, Y. H. Dong, L. M. Wang, *J. Mater. Chem.* **2012**, *22*, 11452.
- [18] Y. S. Su, A. Manthiram, *Nat. Commun.* **2012**, *3*, 1166.
- [19] S. H. Chung, A. Manthiram, *Chem. Commun.* **2014**, *50*, 4184.
- [20] T. G. Jeong, Y. H. Moon, H. H. Chun, H. S. Kim, B. W. Cho, Y. T. Kim, *Chem. Commun.* **2013**, *49*, 11107.
- [21] S. H. Chung, A. Manthiram, *Adv. Mater.* **2014**, *26*, 1360.
- [22] J. Q. Huang, Q. Zhang, H. J. Peng, X. Y. Liu, W. Z. Qian, F. Wei, *Energy Environ. Sci.* **2014**, *7*, 347.
- [23] Z. B. Xiao, Z. Yang, L. Wang, H. G. Nie, M. Zhong, Q. Q. Lai, X. J. Xu, L. J. Zhang, S. M. Huang, *Adv. Mater.* **2015**, *27*, 2891.
- [24] T. H. Zhou, W. Lv, J. Li, G. M. Zhou, Y. Zhao, S. X. Fan, B. L. Liu, B. H. Li, F. Y. Kang, Q. H. Yang, *Energy Environ. Sci.* **2017**, *10*, 1694.
- [25] B. Anasori, M. R. Lukatskaya, Y. Gogotsi, *Nat. Rev. Mater.* **2017**, *2*, 16098.

- [26] L. X. Wang, J. C. Sun, B. Kang, S. Li, S. J. Ji, Z. S. Wen, X. C. Wang, *J. Power Sources* **2014**, 246, 775.
- [27] J. B. Li, G. Y. Xu, E. Y. Sun, Y. Huang, P. F. Becher, *J. Am. Ceram. Soc.* **1998**, 81, 1689.
- [28] L. Shi, Y. L. Gu, L. Y. Chen, Z. H. Yang, J. H. Ma, Y. T. Qian, *Solid State Ionics* **2005**, 176, 841.
- [29] K. Ichikawa, M. Achikita, *Mater. Trans., JIM* **1993**, 34, 718.
- [30] H. H. Crayton, M. C. Gridly, *Powder Metall. Bull.* **1971**, 14, 78.
- [31] P. G. Li, M. Lei, Z. B. Sun, L. Z. Cao, Y. F. Guo, X. Guo, W. H. Tang, *J. Alloys Compd.* **2007**, 430, 237.
- [32] A. Singh, M. H. Modi, P. Rajput, A. K. Sinha, G. S. Lodha, *J. Appl. Phys.* **2015**, 117, 175301.
- [33] M. T. Marques, A. M. Ferrari, J. B. Correia, A. M. B. Rego, R. Vilar, *Mater. Chem. Phys.* **2008**, 109, 174.
- [34] A. Kawase, S. Shirai, Y. Yamoto, R. Arakawa, T. Takata, *Phys. Chem. Chem. Phys.* **2014**, 16, 9344.
- [35] C. Barchasz, F. Molton, C. Duboc, J. C. Leprêtre, S. Patoux, F. Alloin, *Anal. Chem.* **2012**, 84, 3973.
- [36] Q. L. Zou, Y. C. Lu, *J. Phys. Chem. Lett.* **2016**, 7, 1518.
- [37] Q. Pang, D. Kundu, M. Cuisinier, L. F. Nazar, *Nat. Commun.* **2014**, 5, 4759.
- [38] G. M. Zhou, Y. B. Zhao, C. X. Zu, A. Manthiram, *Nano Energy* **2015**, 12, 240.
- [39] Y. Xia, R. Y. Fang, Z. Xiao, H. Huang, Y. P. Gan, R. J. Yan, X. H. Lu, C. Liang, J. Zhang, X. Y. Tao, W. K. Zhang, *ACS Appl. Mater. Interfaces* **2017**, 9, 23782.
- [40] G. M. Zhou, S. F. Pei, L. Li, D. W. Wang, S. G. Wang, K. Huang, L. C. Yin, F. Li, H. M. Cheng, *Adv. Mater.* **2013**, 26, 4.
- [41] Y. S. Su, Y. Z. Fu, B. K. Guo, S. Dai, A. Manthiram, *Chem. Eur. J.* **2013**, 19, 8621.
- [42] X. Ji, L. F. Nazar, *J. Mater. Chem.* **2010**, 20, 9821.
- [43] W. L. Cai, G. R. Li, F. He, L. M. Jin, B. H. Liu, Z. P. Li, *J. Power Sources* **2015**, 283, 524.
- [44] X. N. Li, J. W. Liang, Y. Lu, Z. G. Hou, W. Q. Zhang, Y. C. Zhu, Y. T. Qian, *J. Power Sources* **2016**, 329, 379.
- [45] L. Wang, J. Liu, S. Yuan, Y. Wang, Y. Y. Xia, *Energy Environ. Sci.* **2016**, 9, 224.
- [46] Y. V. Mikhaylik, J. R. Akridge, *J. Electrochem. Soc.* **2004**, 151, 1969.
- [47] C. J. Hart, M. Cuisinier, X. Liang, D. Kundu, A. Garsuch, L. F. Nazar, *Chem. Commun.* **2015**, 51, 2308.
- [48] H. Ryu, H. Ahn, K. Kim, J. Ahn, J. Lee, E. Cairns, *J. Power Sources* **2005**, 140, 365.
- [49] G. Q. Ma, Z. Y. Wen, Q. S. Wang, C. Shen, P. Peng, J. Jin, X. W. Wu, *J. Power Sources* **2015**, 273, 511.
- [50] L. Q. Yang, G. C. Li, X. Jiang, T. R. Zhang, H. B. Lin, J. Y. Lee, *J. Mater. Chem. A* **2017**, 5, 12506.